Remote Sensing of Environment 258 (2021) 112343

Contents lists available at ScienceDirect

Remote Sensing of Environment

journal homepage: www.elsevier.com/locate/rse

SAR-derived flow velocity and its link to glacier surface elevation change and mass balance

Sergey Samsonov [a,*], Kristy Tiampo [b], Ryan Cassotto [b]

[a] Canada Centre for Mapping and Earth Observation, Natural Resources Canada, 560 Rochester Street, Ottawa, ON K1S5K2, Canada
[b] Earth Science & Observation Center, Cooperative Institute for Research in Environmental Sciences, University of Colorado, Boulder, CO 80309, USA

ARTICLE INFO

Editor: Dr. M Wang

ABSTRACT

Modern remote sensing techniques, such as Synthetic Aperture Radar (SAR), can measure the direction and intensity of glacier flow. Yet the question remains as to what these measurements reveal about glaciers' adjustment to the warming climate. Here, we present a technique that addresses this question by linking the SAR-derived velocity measurements with the glacier elevation change and the specific mass balance (i.e. mass balance per unit area). The technique computes the speckle offset tracking results from the north, east and vertical flow displacement time series, with the vertical component further split into a Surface Parallel Flow (SPF) advection component due to the motion along a glacier surface slope and a non-Surface Parallel Flow (nSPF). The latter links the glacier surface elevation change with the specific mass balance and strain rates. We apply this technique to ascending and descending Sentinel-1 data to derive the four-dimensional flow displacement time series for glaciers in southeast Alaska during 2016–2019. Time series extracted for a few characteristic regions demonstrate remarkable temporal variability in flow velocities. The seasonal signal observed in the nSPF component is modeled using the Positive Degree Day model. This method can be used for computing either mass balance or glacier surface elevation change if one of these two parameters is known from external observations.

1. Introduction

In recent years, a variety of modern remote sensing techniques have been used for glacier monitoring, including Synthetic Aperture Radar (SAR) (Rignot 1998; Shepherd et al. 2001; Burgess et al. 2013), Global Navigation Satellite System (GNSS) (van de Wal et al. 2008; Bartholomew et al. 2010), optical imagery (Berthier et al. 2005; Herman et al. 2011; Fahnestock et al. 2016) and unmanned aerial vehicles (Immerzeel et al. 2014). In particular, SAR can measure the direction and intensity of glacier flow. However, it is not clear what these measurements tell us about the glaciologic response to the warming climate. The technique presented here provides, for the first time, important insights into glaciers' dynamic adjustments in response to the changing climate by linking SAR-derived velocity measurements with the glacier elevation change and the specific surface mass balance (i.e. mass balance per unit area). Temporal variations in mass balance distribution are preferred over changes in net balance (i.e. volume change estimates), as the former reacts immediately to climatic shifts and does not decay with time (Gudmundsson and Bauder 1999).

Of the available satellite remote sensing techniques, SAR is the only active sensor with global coverage at high temporal and spatial resolutions that can operate in any weather conditions, day or night (Mohr et al. 1998; Rignot 2002; Joughin 2002). Since its early inception, SAR has been used in glacier monitoring for estimating flow velocities, surface flux, tidal variations, and grounding line behavior (Goldstein et al. 1993; Joughin et al. 1995, 1998; Rignot 1998; Shepherd et al. 2001; Palmer et al. 2010; Minchew et al. 2017). In this study, we utilize ascending and descending Sentinel-1 SAR data acquired during 2016–2019 to study glaciers in southeast Alaska (Fig. 1). This technique can be applied to any moderate-to-high resolution SAR data, including the vast collection of ascending and descending stacks that have been collected for many glaciers around the world since the early 1990s.

The SAR speckle offset tracking (SPO) technique computes displacements in the satellite range and azimuth directions by applying image correlation algorithms to radar backscatter (Michel and Rignot 1999; Gray et al. 2001; Strozzi et al. 2002; Joughin 2002). The precision of this technique depends on the spatial resolution of SAR data and is lower than the precision of differential interferometry (DInSAR) (Strozzi

* Corresponding author.
E-mail address: sergey.samsonov@canada.ca (S. Samsonov).

https://doi.org/10.1016/j.rse.2021.112343
Received 26 July 2020; Received in revised form 26 January 2021; Accepted 3 February 2021
Available online 2 March 2021

et al. 2002). However, SPO processing does not require phase unwrapping, which makes it particularly suitable for measuring very fast glacier flows, as observed in this study.

The technique presented here computes the four-dimensional flow displacement time series and linear flow velocities from one ascending and one descending SAR data set by applying the Multidimensional Small Baseline Subset (MSBAS) methodology (Samsonov 2019; Samsonov et al., 2020a, b). Three orthogonal flow displacement components are calculated (north, east, and vertical) with the vertical component divided into two components: Surface Parallel Flow (SPF) and the non-Surface Parallel Flow (nSPF). SPF characterizes elevation change due to the motion along a glacier surface slope while nSPF characterizes variations due to strain rates and mass balance processes. In comparison to the techniques that compute changes in net mass balance from volume change measurements, for example, by differencing DEMs (Bolch et al. 2011; Kaab et al. 2012; Gardelle et al., 2012), our technique computes temporal variations in mass balance distribution. This allows us to distinguish processes due to accumulation/ablation and advection.

2. Model

Speckle offset tracking (SPO) technique computes from two SAR images offsets in the satellite range and azimuth directions. Range offsets are sensitive to horizontal and vertical motion while azimuth offsets are sensitive to horizontal motion only. By combining range and azimuth offsets from ascending and descending passes, the north (V_n), east (V_e) and vertical (V_v) components of flow velocity can be resolved (e.g. Fialko et al. 2001)

$$\begin{pmatrix} sin(\phi_{asc})sin(\theta_{asc})\partial t_{asc} & -cos(\phi_{asc})sin(\theta_{asc})\partial t_{asc} & cos(\theta_{asc})\partial t_{asc} \\ cos(\phi_{asc})\partial t_{asc} & sin(\phi_{asc})\partial t_{asc} & 0 \\ sin(\phi_{dsc})sin(\theta_{dsc})\partial t_{dsc} & -cos(\phi_{dsc})sin(\theta_{dsc})\partial t_{dsc} & cos(\theta_{dsc})\partial t_{dsc} \\ cos(\phi_{dsc})\partial t_{dsc} & sin(\phi_{dsc})\partial t_{dsc} & 0 \end{pmatrix} \begin{pmatrix} V_n \\ V_e \\ V_v \end{pmatrix} = \begin{pmatrix} RO_{asc} \\ AO_{asc} \\ RO_{dsc} \\ AO_{dsc} \end{pmatrix} \quad (1)$$

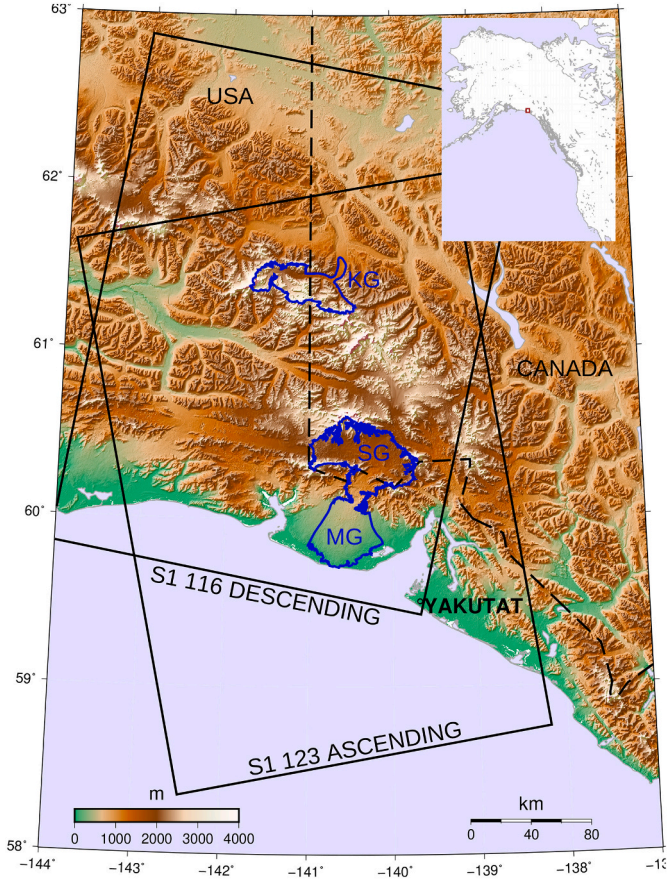

Fig. 1. Area of interest is Saint Elias Mountains in southeastern Alaska and southwestern Yukon. Outlines of ascending (track 123) and descending (track 116) Sentinel-1 swaths are shown in black. Background is 30 m Advanced Spaceborne Thermal Emission and Reflection Radiometer (ASTER) digital elevation model (DEM). Historic climate data was acquired by Yakutat weather station. Outlines of Klutaln KG, Seward (SG), and Malaspina (MG) glaciers are shown in blue (downloaded from GLIMS Glacier Database at http://glims.colorado.edu/glacierdata). (For interpretation of the references to colour in this figure legend, the reader is referred to the web version of this article.)

Here ϕ and θ are the azimuth and incidence angles and RO and AO are the range and azimuth offsets computed over the time interval ∂t on ascending and descending passes. It is common for ascending and descending SAR images to be acquired at different times and with different time intervals (e.g. some acquisitions can be missed). In such cases, the 3D flow velocity vector can be reconstructed only by assuming that it remains constant during the ascending and descending acquisitions. Solving for components of flow velocity instead of flow displacement allows us to combine ascending and descending range and azimuth offsets acquired over slightly different time intervals ∂t_{asc} and ∂t_{dsc}. The set of eqs. (1) is over-determined; it contains four equations but only three unknowns.

The glacier kinematic boundary condition at the surface relates the rate of change of surface elevation $\dot{s} = \frac{\partial s}{\partial t}$, the vertical ice-particle (pole) velocity V_v, the horizontal velocity vector $\boldsymbol{V_h}$, the surface slope ∇s, the specific mass balance rate $\dot{b} = \frac{1}{\rho}\frac{\partial b}{\partial t}$ and the the column-average density ρ (Reeh et al. 1999; Beedle et al. 2014)

$$\dot{s} = V_v + \dot{b} - \boldsymbol{V_h}\nabla s. \quad (2)$$

Here, we invoke Sorge's Law of constant density (Cogley et al. 2011) within a column of ice, neglect the vertical profile of velocity, and assume that a thickness change can be converted to an equivalent mass

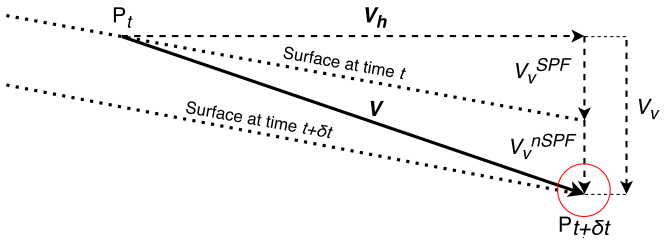

Fig. 2. Kinematic boundary condition at surface. Ice parcel, located at P_t at time t moves to $P_{t+\partial t}$ at time $t+\partial t$ with velocity $\boldsymbol{V}$, with horizontal component $\boldsymbol{V_h}$ and vertical component V_v. Vertical component V_v consists of $V_v^{SPF} = \boldsymbol{V_h}\nabla s$ and $V_v^{nSPF} = \dot{s} - \dot{b}$ components. Red circle indicates error in location of ice parcel at $t+\partial t$ due to potential change in penetration depth. (For interpretation of the references to colour in this figure legend, the reader is referred to the web version of this article.)

change by multiplying by the column-average density.

The vertical ice-particle (pole) velocity V_v is then equal to

$$V_v = \boldsymbol{V_h}\nabla s + \dot{s} - \dot{b}. \tag{3}$$

The SAR-derived vertical flow velocity (that consists of SPF and nSPF components, Fig. 2) is the vertical ice-particle (pole) velocity; therefore, it follows that

$$V_v = V_v^{SPF} + V_v^{nSPF}, \quad where \quad V_v^{SPF} = V_h \nabla s, \quad V_v^{nSPF} = \dot{s} - \dot{b}. \tag{4}$$

By combining (1, 4), north V_n, east V_e, vertical SPF V_v^{SPF} and vertical non-SPF V_v^{nSPF} components of flow velocity can be resolved

$$\begin{pmatrix} sin(\phi_{asc})sin(\theta_{asc})\partial t_{asc} & -cos(\phi_{asc})sin(\theta_{asc})\partial t_{asc} & cos(\theta_{asc})\partial t_{asc} & cos(\theta_{asc})\partial t_{asc} \\ cos(\phi_{asc})\partial t_{asc} & sin(\phi_{asc})\partial t_{asc} & 0 & 0 \\ sin(\phi_{dsc})sin(\theta_{dsc})\partial t_{dsc} & -cos(\phi_{dsc})sin(\theta_{dsc})\partial t_{dsc} & cos(\theta_{dsc}) & cos(\theta_{dsc})\partial t_{dsc} \\ cos(\phi_{dsc})\partial t_{dsc} & sin(\phi_{dsc})\partial t_{dsc} & 0 & 0 \\ \frac{\partial s}{\partial X_n} & \frac{\partial s}{\partial X_e} & -1 & 0 \end{pmatrix} \begin{pmatrix} V_n \\ V_e \\ V_v^{SPF} \\ V_v^{nSPF} \end{pmatrix} = \begin{pmatrix} RO_{asc} \\ AO_{asc} \\ RO_{dsc} \\ AO_{dsc} \\ 0 \end{pmatrix}, \tag{5}$$

where $\frac{\partial s}{\partial X_n}$ and $\frac{\partial s}{\partial X_e}$ are the first central derivatives along the north and east directions, respectfully. The set of eqs. (5) is balanced; it contains four equations and four unknowns.

The original MSBAS technique was developed to compute displacement time series by simultaneously processing heterogeneously-acquired ascending and descending DInSAR data. Depending on the variety of data and chosen processing parameters, MSBAS can compute either 1D (line-of-sight), 2D (east and vertical), or SPF-constrained 3D (north, east, vertical) displacement time series (Samsonov and d'Oreye, 2012, 2017; Samsonov 2019; Samsonov et al., 2020a).

In the case of speckle offset tracking, the original MSBAS technique can be modified to utilize: (i) the left matrix in (1) when solving for three components of flow velocity (Samsonov et al., 2020b), or (ii) the left matrix in (5) when solving for four components of flow velocity (this study). In matrix form, the latter problem and its solution can be written as follows

$$\begin{pmatrix} A \\ H \\ \lambda L \end{pmatrix} \begin{pmatrix} V_n \\ V_e \\ V_v^{SPF} \\ V_v^{nSPF} \end{pmatrix} = \begin{pmatrix} RO \\ AO \\ 0 \\ 0 \end{pmatrix}, \quad \begin{pmatrix} V_n \\ V_e \\ V_v^{SPF} \\ V_v^{nSPF} \end{pmatrix} = \begin{pmatrix} A \\ H \\ \lambda L \end{pmatrix}^{+} \begin{pmatrix} RO \\ AO \\ 0 \\ 0 \end{pmatrix}, \quad D_j^{i+1} = D_j^i + V_j^i \partial t^i, \quad j = n, e, v^{SPF}, v^{nSPF} \tag{6}$$

where A is the geometry matrix, H is the topography matrix, L is the Tikhonov regularization matrix multiplied by the regularization parameter λ, RO and AO are the known range and azimuth offset matrices, V^i is the flow velocity and D^i is the flow displacement matrices at time epoch i. Four unknown components of flow velocity for each time epoch are found by inverting (6) using singular value decomposition. Time series of four flow displacement components are computed by numerical integration. Finally, four components of the linear flow velocity are computed by fitting a straight line to the corresponding flow displacement time series using the linear regression.

The Tikhonov regularization matrix L can be of either zeroth, first, or second-degree (Samsonov and d'Oreye, 2017; Samsonov 2019), and the regularization parameter λ can be selected, for example, with the L-curve method (Hansen and O'Leary, 1993).

2.1. Positive degree day model

Positive Degree Day (PDD) models provide estimates of glacial surface melting due to exposure to warm atmospheric temperatures (Braithwaite and Zong 2000; Vaughan 2006). It assumes that for each positive degree Celsius a certain depth of snow, measured in millimeters water equivalent (mm w.e.), is melted. This model takes into account the amount of energy available for melting (the total sum of daily average temperatures above 0°C) and the melting rate per degree (the degree-day factor). In our case, this model can be written as follows

$$\begin{gathered} T(t) = \frac{T_{min}(t) + T_{max}(t)}{2} + T_0 \\ \gamma(t) = \sum_{t=t_0}^{t} \alpha(T(t))T(t), \quad \alpha(T(t)) = \begin{cases} 1, T(t) > 0^{\circ}C \\ 0, T(t) < 0^{\circ}C \end{cases} \\ D(t) = -\beta k_0 \gamma(t) = -k\gamma(t), \end{gathered} \tag{7}$$

where $T(t)$ is the mean daily temperature at a glacier, computed as an average of the daily minimum $T_{min}(t)$ and the daily maximum $T_{max}(t)$ at the Yakutat weather station plus T_0, a constant offset between the mean daily temperature at the Yakutat weather station and a glacier; $\gamma(t)$ is the cumulative positive degree day sum since $t_0 = 20161120$ (i.e. start of SAR-derived time series); $D(t)$ is the cumulative flow displacement equivalent of D_v^{nSPF} from (6); k_0 is the degree-day factor; β is the parameter that relates the actual depth of melted snow with the SAR-derived vertical nSPF flow displacement.

The adiabatic lapse rate can be estimated from various models. However, these models do not account for local effects of surface temperature changes related to near-surface wind direction and strength,

Table 1
Sentinel-1 SAR data used in this study, where θ is incidence and ϕ is azimuth angles.

	Span	θ°	ϕ°	SLC images
Sentinel-1 track 123 (asc)	20161220–20191217	39	342	79
Sentinel-1 track 116 (dsc)	20161207–20191222	39	198	85

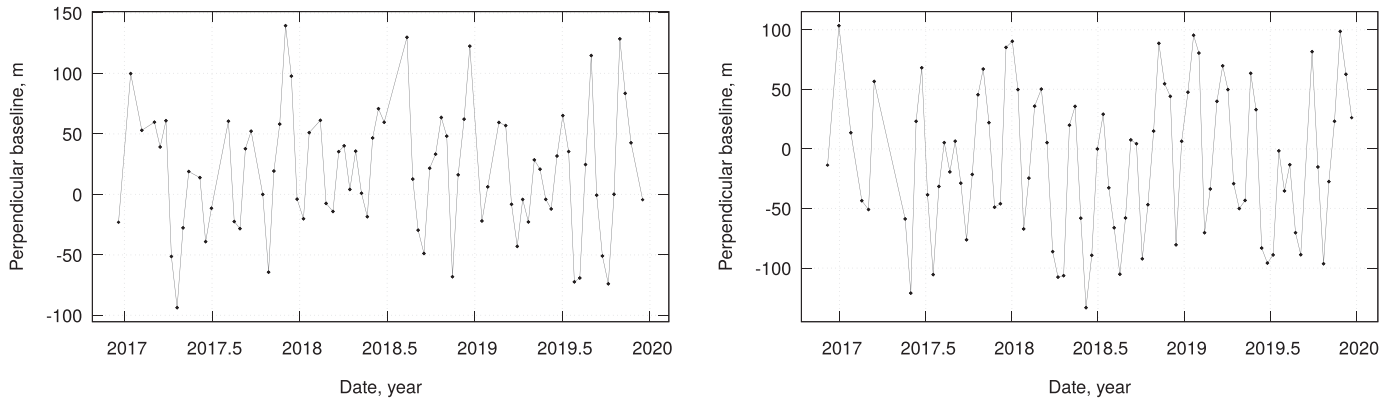

(a) Ascending Sentinel-1 track 123 (b) Descending Sentinel-1 track 116

Fig. 3. Spatial and temporal baselines of Sentinel-1 pairs used in this study.

aspect, solar exposure, and surface absorption/reflectivity. Consequently, T_0 is difficult to parameterize and must be modeled.

The parameter β relates the actual depth of melted snow predicted by the PDD model with the SAR-derived vertical nSPF flow displacement. An estimation of this parameter requires knowledge of SAR penetration depths for various glaciers in different climatic conditions and snow densities, which is beyond the scope of this study. Instead, it is assumed to be equal to one, which changes the value of the degree-day factor k_0. Therefore, instead of solving for two parameters, β and k, we solve for one parameter, the SAR-derived degree-day factor $k = \beta k_0$.

The positive degree day model is fitted to SAR-derived vertical nSPF flow displacement time series at regions that show seasonal variability producing optimal T_0 and k. The actual values of T_0 and k are not used in this study because they reflect measurements at the penetration depth rather than at the surface. Instead, we investigate if seasonal variability observed in the SAR-derived time series can be fully explained by seasonal variability in the surface air temperature.

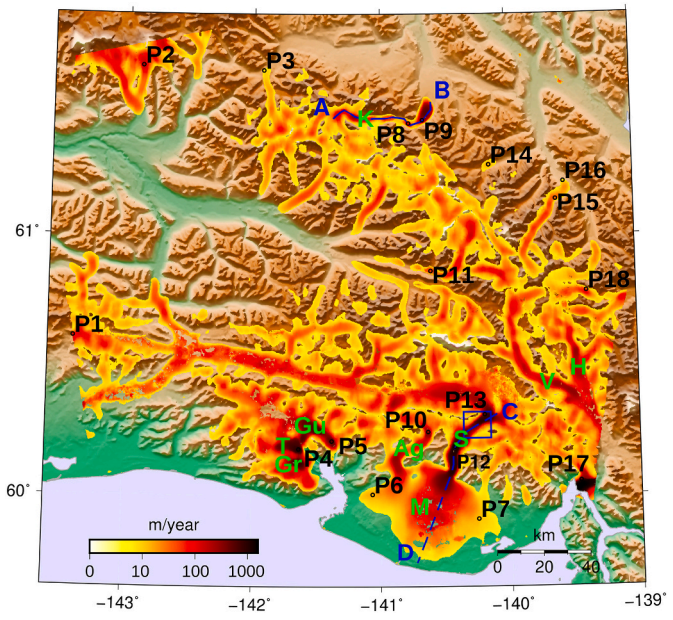

Fig. 4. Magnitude of mean 3D velocity vector averaged over observation period and plotted using base-10 log scale. Values less than 5 m/year were clipped. Background is 30 m ASTER DEM. Time series for 5 × 5-pixel regions P1-P18 are shown in Fig. 10. AB is profile along Klutlan glacier, CD is profile along Seward and Malaspina glaciers. Region outlined by blue rectangle is shown in Fig. 9. Glaciers: Ag-Agassiz, Gr-Grotto, Gu-Guyot, H-Hubbard, M-Malaspina, S-Seward, T-Tsaa, V-Valerie. (For interpretation of the references to colour in this figure legend, the reader is referred to the web version of this article.)

3. Data

In this study, we used 158 ascending (track 123) and 170 descending (track 116) Sentinel-1 single-look complex (SLC) images acquired during 7 December 2016–17 December 2019 and downloaded from the NASA Distributed Active Archive Center (DAAC) operated by the Alaska Satellite Facility (ASF) (Table 1). Two ascending and two descending frames along the azimuth directions were concatenated, resulting in 79 and 85 swaths, respectfully. Ascending and descending sets were processed individually using GAMMA software (Wegmuller and Werner 1997) that produced range and azimuth offsets for consecutive pairs (Fig. 3). Offsets were spatially filtered, geocoded using a 30 m ASTER DEM and resampled to a common grid with a ground resolution of about 200 m.

We used Generic Mapping Tools (GMT) commands to filter a DEM and compute surface slopes. An ASTER 30 m DEM was spatially filtered with Gaussian weights and a 6-sigma diameter of 2 km and used to calculate the first central derivatives along the north ($\frac{\partial s}{\partial X_n}$) and east ($\frac{\partial s}{\partial X_e}$) directions.

Ascending and descending range and azimuth offsets and topographic derivatives were used as inputs to the MSBAS algorithm to produce north, east, vertical SPF and vertical nSPF flow displacement time series and linear flow velocities.

We downloaded daily climate data during 7 December 2016–17 December 2019 for the Yakutat weather station from the National Oceanic and Atmospheric Administration National Centers for Environmental Information (NOAA-NCEI, https://www.ncdc.noaa.gov).

4. Results

The magnitude of the linear flow velocity $\sqrt{{V_n}^2 + {V_e}^2 + \left(V_v^{SPF} + V_v^{nSPF}\right)^2}$ plotted using a base-10 log scale overlays the 30 m ASTER DEM in Fig. 4 with values below 5 m/year removed. Eighteen 5× 5-pixel regions P1-P18 are marked as black dots. For these characteristic regions, flow displacement time series are provided in Fig. 10. The largest value of 1650 m/year is observed on the Seward glacier near region P12.

Linear flow velocity vectors along the Klutlan glacier (profile AB in Fig. 4) are plotted in Fig. 5 as arrows at the glacier surface. The vectors are produced from the magnitude of horizontal ($\sqrt{{V_n}^2 + {V_e}^2}$) and vertical flow components ($V_v^{SPF} + V_v^{nSPF}$). To produce the topographic and velocity slopes without angular distortion, the vertical and horizontal axes were scaled equally, which produced a disproportionally long

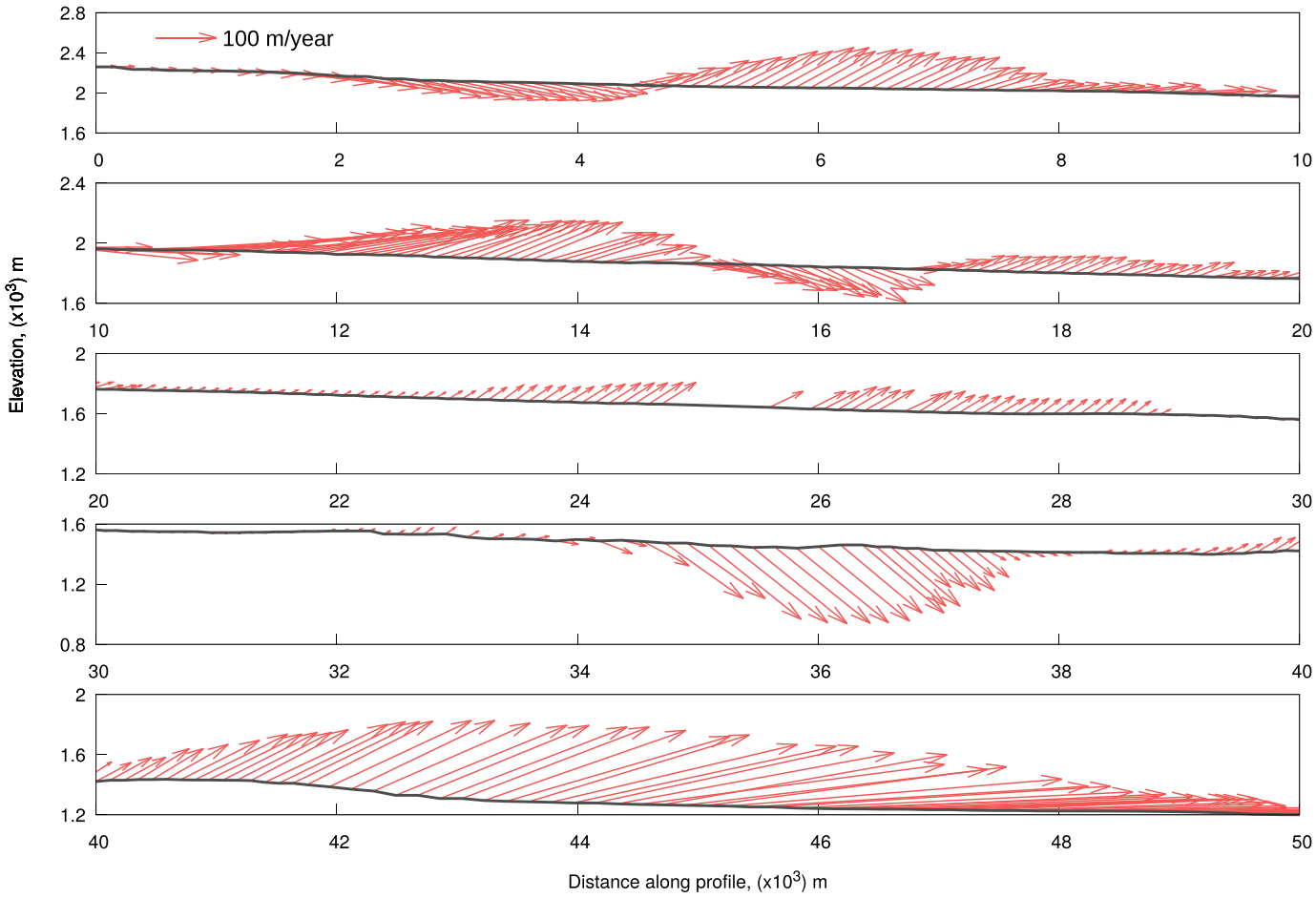

Fig. 5. Elevation and flow velocity averaged over observation period for Klutlan glacier along profile AB. To display topographic and velocity slopes without angular distortion, long profile AB is folded five times so each subplot maps consecutive 10,000 m segment with vertical range of 800 m (e.g. first segment: 0–10,000 m, second segment 10,000–20,000 m, etc). Magnitude of velocity vector is exaggerated relative to distance along profile and elevation.

figure with a 50 km horizontal range but only 800 m of range in the vertical. For aesthetics, the continuous profile was broken up into five equal-length segments of 10 km each, with the first segment spanning the initial 0–10 km of the profile AB and the last segment spanning the final 40–50 km. In addition, we increased the length of velocity vectors by a factor of 5, such that 200 m/year corresponds to 1000 m of length along the profile. The magnitude and direction of flow velocities vary significantly along this profile, with flow direction rarely parallel to the glacier surface. Multiple regions of the upward motion are followed by regions of downward motion, where velocity slope is significantly steeper than topographic slope.

The linear flow velocity vectors extracted along the Seward and Malaspina Glaciers (profile CD in Fig. 4) are plotted in Fig. 6 as arrows at the glacier surface. Similar to Fig. 5, the profile was arranged to produce seven segments of 10 km each. The largest magnitude of flow velocity (570 m/year) is observed in the middle of the profile and variability in flow direction is less extreme. Downward motion, where velocity slope is significantly steeper than topographic slope, is predominant.

The SPF and nSPF components of vertical flow velocity overlay the 30 m ASTER DEM in Figs. 7-8. The colour scales in these figures were saturated to ±20 m/year range while actual values ranged from −190 to +28 and − 396 to 392 m/year range, and mean values were − 2.6 ± 6.6 and − 3.2 ± 13.6 m/year, respectfully. As expected, the magnitude of the vertical SPF component varies moderately with a predominantly downward flow direction. In contrast, the magnitude and direction of the vertical nSPF component show larger variability along some glaciers.

To emphasize the vast amount of information presented in Figs. 4, 7-8 and outline the limitations of this technique, we plotted a region of the Seward glacier where large nSPF velocity is observed at full resolution. Fig. 9 shows the SAR intensity, magnitude of velocity vectors, the SPF, and nSPF components of flow. Each panel additionally contains an insert that shows topography along the dashed-line profile.

The highest magnitudes in velocity (panel b) are located at the top part of the glacier (in the black, top-right corner of the panel), followed by small values (center) and moderate values (bottom-left corner). Since the amount of ice passing through this part of a glacier remains nearly constant during the observation period, the fast horizontal flow (top-right corner) must be accommodated by the vertical flow (center). Indeed, the flow direction along the dashed-line profile changes from nearly parallel to the surface to more downward, as shown in the nSPF component (panel c), the profile CD (Fig. 6), and two supplementary animations. Such a flow pattern is likely related to the unique configuration of the glacier, including bed geometry and topography, and inflow pattern.

The fastest SPF motion is observed in regions of steep topography (panel c). Note that the largest nSPF values (center of the panel) are observed in a region of shallow topography. Here the computed SPF component is small because $\nabla s \approx 0$ and the vertical flow of ice is governed mainly by variations in strain rates than gravitational sliding. The presence of a narrow channel with a large nSPF velocity (top-right corner) indicates that the flow pattern is not uniform across the valley.

The four components of the flow-displacement time series for regions P1-P18 are shown in Fig. 10, arranged by longitude from west to east.

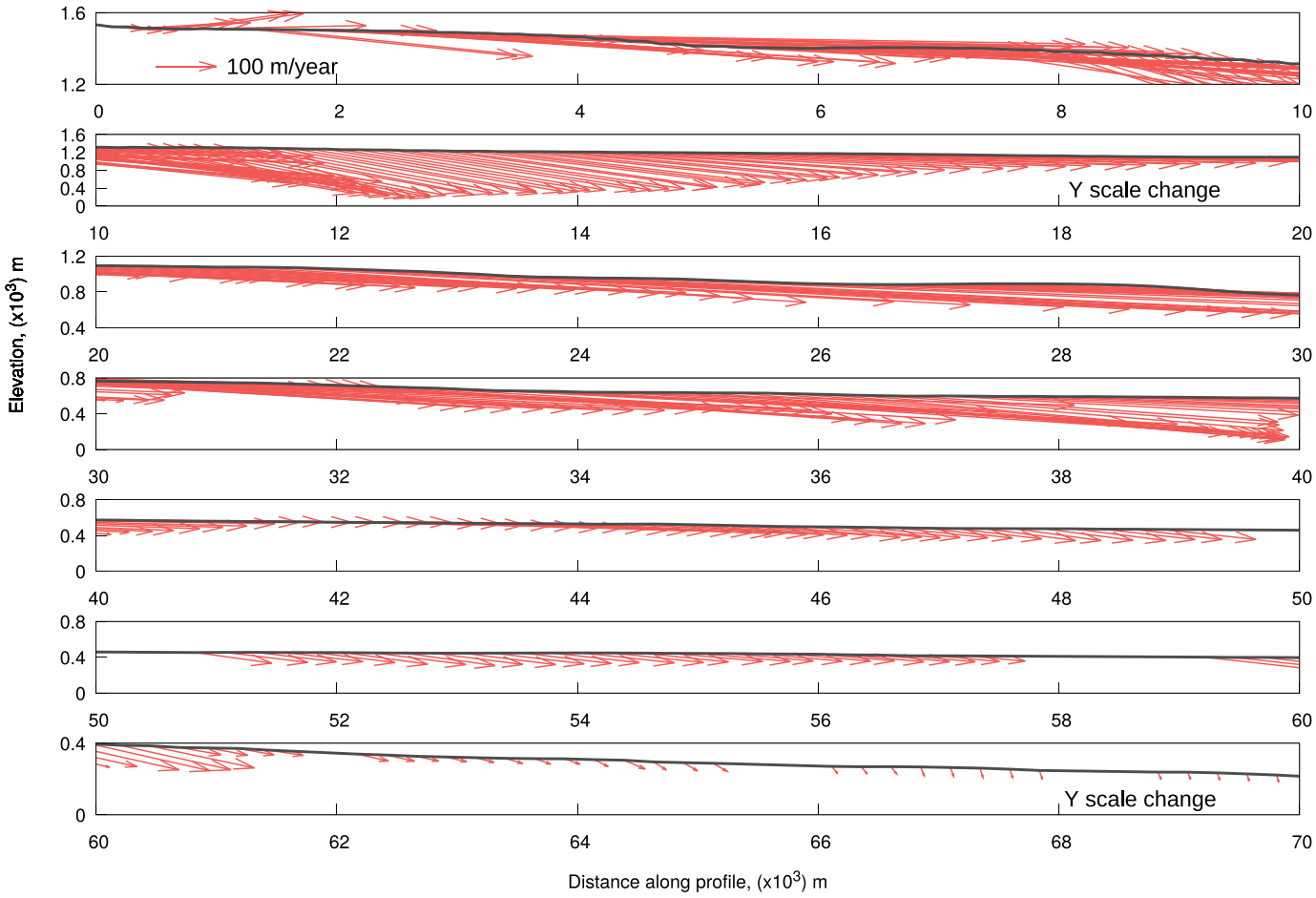

Fig. 6. Elevation and flow velocity averaged over observation period for Seward and Malaspina glaciers along profile CD. To display topographic and velocity slopes without angular distortion, long profile CD is folded seven times so each subplot maps consecutive 10,000 m segment with vertical range of 800 m (e.g. first segment: 0–10,000 m, second segment 10,000–20,000 m, etc). Magnitude of velocity vector is exaggerated relative to distance along profile and elevation.

These 18 regions were selected manually to demonstrate a variety of signals that can be observed using this technique. Very fast flow is observed at P4, P5, P10, P12, P13, and P17. Seasonal variability in vertical nSPF component is observed at P1, P3, P6, P7, P13, P14, P16, P17, and P18. Non-stationary flow is observed at P8, P9, P11, and P14. Error bars in these time series measure deviation from a mean value within a 5×5 pixels window; which is due only in part to the measurement precision.

4.1. Positive degree day modeling results

The Positive Degree Day model was fitted to the vertical nSPF component of flow displacement time series observed at P3, P6, P7, and P16, which experience significant displacements during warm seasons and minimal displacement during cold seasons (Fig. 11). The values of T_0 and k produced by modeling are shown in Table 2. The fit is very good at P3, P6, and P7, but the model at P16 does not capture periods of upward flow observed during cold seasons.

Regions P1 and P17 experience upward flow during cold seasons, followed by the absence of flow during warm seasons. For these regions, we assumed a linear upward trend modulated by the signal produced by the PDD model. This approach produced erroneous T_0 and k values. Instead, since P1 is located at approximately the same elevation as P3, we used P3's parameters at P1 and solved for a rate only. A similar approach was applied to P17, using model parameters from P7. The seasonal flow pattern cannot be explained by the seasonal variability in the surface air temperature at these two regions, as predicted by the PDD model. Estimation of the standard deviation of the model parameters was performed using the bootstrap method with random sampling performed one hundred times.

5. Discussion

The novel technique presented here computes flow displacement time series and linear flow velocities from ascending and descending range and azimuth offsets. Flow displacement time series can be computed from as little as two ascending and two descending SAR images acquired over the common time period. However, more data allows computing longer time series and mean velocities with higher precision.

We split the vertical component of motion into the surface parallel flow (SPF) and non-surface parallel flow (nSPF) to evaluate the dynamic ice processes that drive surface elevation changes and, ultimately, glacier mass distribution. In our previous study, we showed that SAR-derived measurements in fixed geophysical space (i.e. an Eulerian representation) are not equivalent to the GNSS-derived time series that track individual receivers mounted to non-stationary geophysical surfaces (i.e. a Lagrangian representation) (Samsonov et al., 2020b). In the Lagrangian representation, displacement time series describe a trajectory of an object in space as a function of time, while the Eulerian displacement time series describe the flux (of ice, rock, etc.) at the surface. To emphasize this difference we use the *flow displacement* terminology. The availability of range and azimuth ascending and descending offsets produced by the speckle offset tracking technique allows us to resolve all (four) displacement components with equally

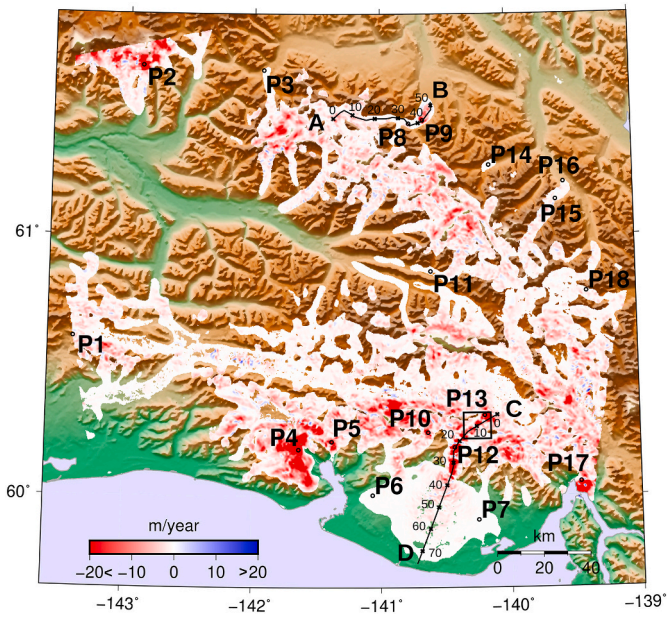

Fig. 7. Surface Parallel Flow (SPF) component of vertical flow velocity averaged over observation period. Time series for 5 × 5-pixel regions P1-P18 are shown in Fig. 10. AB is profile along Klutlan glacier, CD is profile along Seward and Malaspina glaciers, with 10 km markers along profiles shown in pink. Region outlined by black rectange is shown in Fig. 9. Scale was clipped to [−20; 20] m/year, while actual values are in range [−190; 28] m/year. Mean value is −2.6 ± 6.6 m/year. Negative values describe downward vertical motion. (For interpretation of the references to colour in this figure legend, the reader is referred to the web version of this article.)

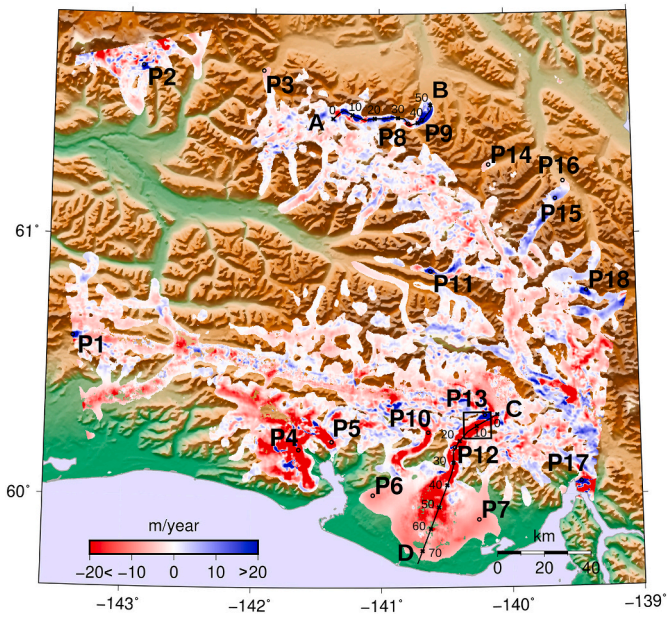

Fig. 8. Non-Surface Parallel Flow (nSPF) component of vertical flow velocity averaged over observation period. Time series for 5 × 5-pixel regions P1-P18 are shown in Fig. 10. AB is profile along Klutlan glacier, CD is profile along Seward and Malaspina glaciers, with 10 km markers along profiles shown in pink. Region outlined by black rectangle is shown in Fig. 9. Scale was clipped to [−20; 20] m/year, while actual values are in range [−396; 392] m/year. Mean value is −3.2 ± 13.6 m/year. Negative values describe downward vertical motion. (For interpretation of the references to colour in this figure legend, the reader is referred to the web version of this article.)

high precision. When only one, either ascending or descending set is available, MSBAS can be used to compute time series of three displacement components, assuming the SPF constraint. When flow velocities are below the precision of the speckle offset tracking technique, ascending and descending DInSAR data can also be used in MSBAS to compute time series of three displacement components assuming the SPF constraint (Samsonov 2019; Samsonov et al., 2020a). In this study, we showed that glacier flow is often non-surface-parallel. In those cases, the SPF constraint-related techniques would produce inaccurate results without even hinting that SPF constraint may be inapplicable. The acquisition of SAR data is therefore warranted for all glaciers worldwide for ascending and descending orbits simultaneously.

While the precision of individual offset maps can be estimated as 1/10–1/30 of the SAR resolution or about 0.2 m in range and 1 m in azimuth (Strozzi et al. 2002), these values are almost irrelevant given the large number of offset maps used in this study and the large magnitude of the flow. This is somewhat analogous to the precision of GNSS-derived deformation rates, which largely depend on the length of time series rather than the precision of individual GNSS measurement. The precision of vertical flow velocity measurements (Figs. 7-8) is generally high, judging by the presence of very little scattering in the flow displacement time series (e.g. Figs. 10-11). The statistical parameters are estimated by assuming a linear model. The average standard deviation and the coefficient of determination (R^2) for the SPF component are 0.03 m/year and 0.91, and the nSPF component are 0.14 m/year and 0.75. The various measurement and processing biases, however, can potentially affect the absolute accuracy of the flow displacement and velocity measurements. An animation in supplemental materials shows the instantaneous velocities at each time step for the entire region. Annual or any other duration (monthly, quarterly) velocities can also be computed from our flow displacement time series by aggregating time series at different intervals.

The penetration depth likely changes throughout the year due to seasonal temperature changes but this change is small over 6 to 12 days, over which the individual offset maps are computed. The error due to the seasonal variability in penetration depth is removed by differencing primary and secondary observations. This can be deduced from observing seasonally correlated signals only in a few regions (at low and high elevations). Higher temperatures during summer would result in higher water content and less penetration depth, which would appear as an upward movement in the flow displacement time series. We, however, observe downward motion during summer.

The radar penetration depth could also change throughout the day due to surface melt and meltwater percolation variations. Ascending and descending data is acquired at different times; it is processed separately and combined only during MSBAS analysis. Any error due to diurnal variations in penetration depth is also removed by differencing primary and secondary observations since both images are acquired at precisely the same time of day.

For computing the individual offset maps, we perform cross-correlation analysis using a large window equal to 256 × 256 pixels. This approach allows us to measure the predominant displacement and velocity over the entire resolution cell. The smaller subregions of the resolution cell may, however, experience different, usually larger, flow displacements. We further apply the 2D spatial filtering to remove noise and to get a regional representation of the motion. The spatial filtering, however, reduces velocity in the center of a glacier while it increases velocity along the boundaries (i.e. known Gaussian blurring effect in image processing). During the inversion performed with the MSBAS method, we also apply Tikhonov regularization that manifests as low-pass temporal filtering. The regularization, however, reduces the temporal resolution while increasing the precision of the overall trend determination.

In this study, we used the ASTER DEM with one arc-second latitude and longitude postings (approximately 30 m) and vertical accuracy of approximately 10 m. This DEM was generated from 1,264,000 Level-1A

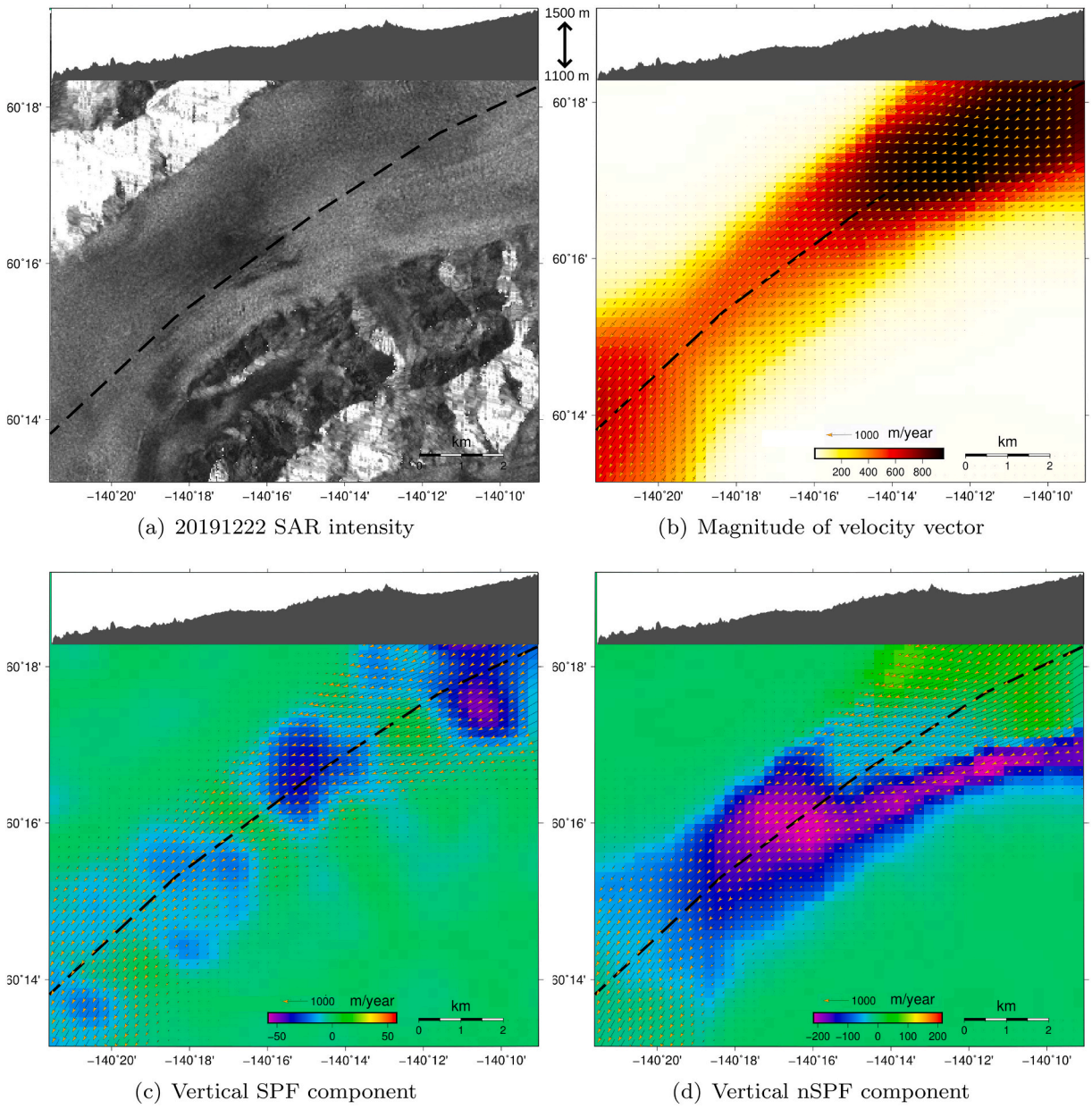

Fig. 9. Area on Seward glacier that exhibits large vertical nSPF component (enlarged from Figs. 4, 7-8). Vectors show direction and magnitude of horizontal velocity components. Elevation profile along black dashed line is shown as insert in each panel.

scenes acquired during March 1, 2000 – November 30, 2007 (Abrams et al. 2020). The DEM was downsampled to approximately 200 m resolution to match the resolution of SAR-derived offset maps. On the release date, the precision of the DEM-derived first central derivatives along the north and east directions was about 1%. Since then, precision has likely decreased due to naturally occurring processes. Elevation change due to the melting of these glaciers likely does not exceed 2 m/year (Sauber et al. 2005) except for small areas. Such elevation change does not result in measurable slope change over the scale of these glaciers. Glacier slope change due to surging or calving activities can be significantly larger; however, it affects only a few small areas and is somewhat random in time. Errors in slope measurements do not affect the precision of the horizontal components of a flow velocity, except for geocoding precision, or the precision of the total vertical component (i.e. $V_v^{SPF} + V_v^{nSPF}$). The individual vertical components are affected by errors in slope measurements in a linear way. For this regional study, as a first-order approximation, the described above slope precision-related effects can be neglected.

The best approach for estimating the absolute measurement accuracy is by comparing these remote-sensing measurements with ground-based measurements (Gudmundsson and Bauder 1999). Such measurements unfortunately are not available for this region during this period. It seems reasonable to assume that to avoid biased estimation of either mass balance distribution or glacier surface elevation change, the known dataset needs to be processed using spatial filtering similar to the SAR-derived results.

Our surface-derived methods specifically measure changes in the vertical flow of ice in an Eulerian reference frame, values that can be used to characterize the processes that ultimately drive ice thickness variations. The conservation of mass requires that the thickness of a column of glacier ice (h) be governed by three processes: strain rates, mass balance (accumulation and melt), and the advection of ice (Amundson and Truffer, 2010); therefore, $\dot{h} = h\dot{\varepsilon}_{zz} + \dot{b} - V_h \nabla h$, where $\dot{\varepsilon}_{zz}$ is the depth-averaged vertical normal strain rate. The SPF component

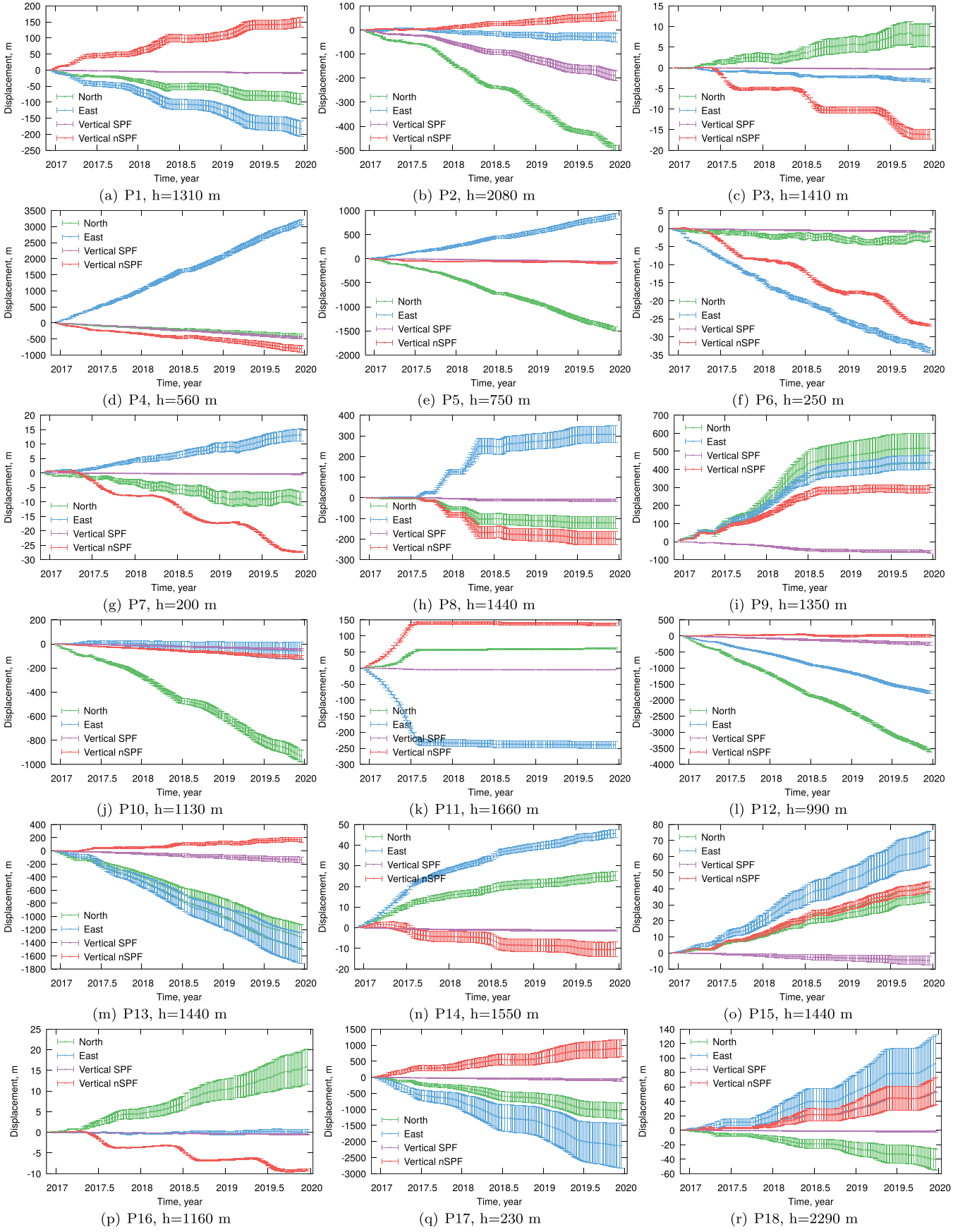

Fig. 10. Flow displacement time series for 5 × 5-pixel regions P1-P18, which locations are shown in Figs. 4-8.

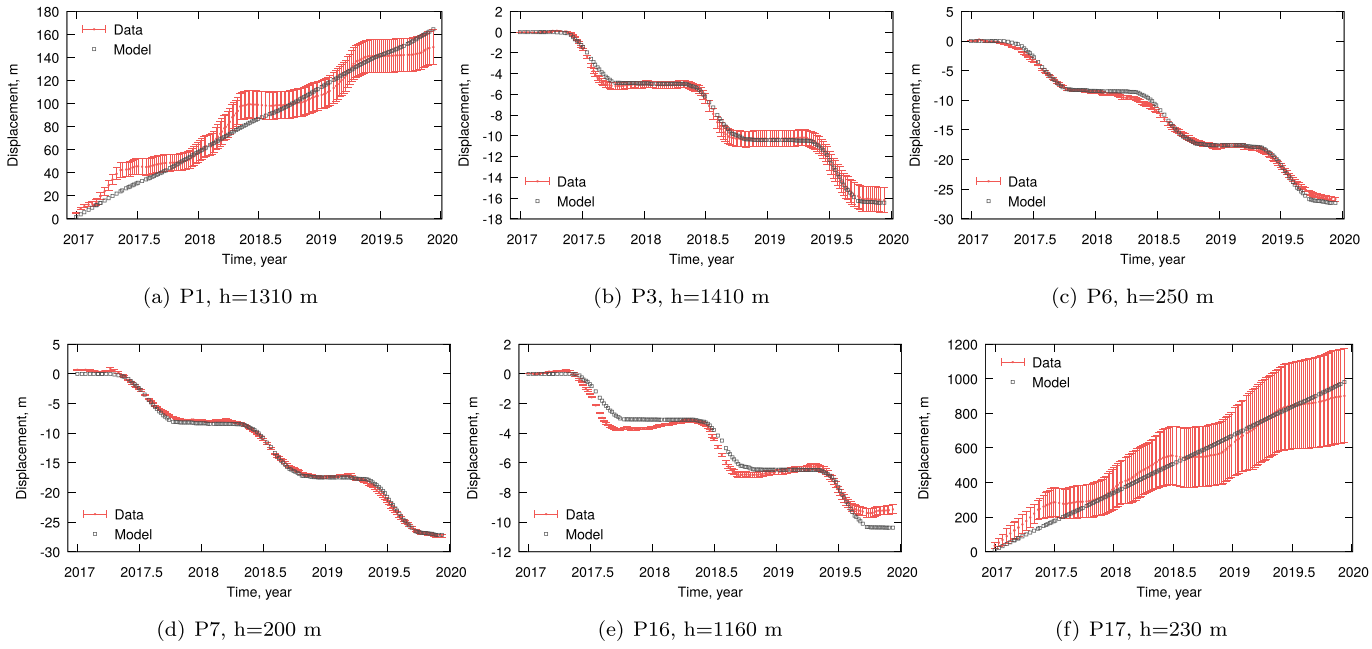

Fig. 11. Time series of vertical nSPF flow velocity for selected 5 × 5-pixel regions P1, P3, P6, P7, P16, and P17. Best fit PDD model was computed for regions P3, P6, P7, and P16 experiencing downward motion. Variability in vertical nSPF flow velocity at these regions is largely affected by seasonal temperature fluctuations. At P1 and P16 linear component was added and PDD model parameters were taken from nearby regions P3 and P7, located at similar elevations. At these regions experiencing upward motion, seasonal flow patterns cannot be explained by seasonal temperature fluctuations.

Table 2
Estimations of PDD model parameters. At P1 and P17 linear component was added and PDD model parameters were taken from nearby regions P3 and P7, located at similar elevations.

Region	*Elevation, m*	T_0, °C	*k, mm w. e.* $^\circ C^{-1} day^{-1}$	V_{nSPF}, *m/year*
P1	1310	−5.8 ± 0.2 (from P3)	7.1 ± 0.3 (from P3)	61 ± 2
P3	1410	−5.8 ± 0.2	7.1 ± 0.3	–
P6	250	−3.9 ± 0.3	8.1 ± 0.4	–
P7	200	−4.1 ± 0.2	8.3 ± 0.2	–
P16	1160	−6.8 ± 0.1	5.7 ± 0.1	–
P17	230	−4.1 ± 0.2 (from P7)	8.3 ± 0.2 (from P7)	339 ± 7

assumes motion parallel to the bedrock surface and thus reflects vertical changes in ice flow due to the advection of ice along the surface. The nSPF component is driven by variations in mass balance $\dot{b}$ and a residual change in surface elevation $\dot{s}$. Assuming that $\dot{s} = \dot{h}$ and $\nabla s = \nabla h$ (i.e. neglecting changes in bedrock due to the ice thickness change), it follows that $V_v^{nSPF} = h\dot{\varepsilon}_{zz}$, demonstrating a dependence of V_v^{nSPF} variations on strain rates.

Ice is incompressible, meaning variations in horizontal strain rates along a glacier directly affect vertical strain rates. When integrated over the full thickness of an ice column, these result in variations in the thickness of that column. A true estimate of ice advection variations requires precise knowledge of ice thickness and therefore the glacier bed. Above we assumed that advection of the ice column was fully captured by measurements of surface advection and that motion was parallel to the bedrock surface. This inherently assumes that the bed and surface geometries are equal and therefore are entirely captured by the SPF component. A detailed bed elevation map that could be used to validate this is non-existent for this region. Nevertheless, this assumption is likely inaccurate because local variations in bed geometry are not captured in DEMs of glacier surfaces. Small scale variations in ice thickness are likely to occur as ice slabs are rarely perfectly parallel in reality. We note that our methods are only valid at the surface and that small variation in bed geometry and vertical strain within the ice column preclude our methods from completely isolating these components. However, because the majority of internal deformation occurs near the bed (Glen 1955) and glacier slopes reflect large scale variations in bed topography, our attempt to delineate these components is a good first approximation that is useful for characterizing underlying ice dynamic processes.

Our techniques allow the ice dynamic processes that drive ice thickness variations to be parsed. Overall, SPF values are predominately negative throughout the region (Fig. 7). The mean SPF is −2.6 m/year; however, the values are heavily skewed negative and range from −190 to 28 m/year. This suggests that advective processes contribute more towards the thinning of ice columns than towards thickening. In general, the highest SPF rates occur near glacier centers (Fig. 7) where the magnitude of 3D flow is greatest (Fig. 4) and ice is typically thickest. Regionally, the highest SPF rates occur along the middle to upper reaches of the Seward, Guyot, Grotto, and Tsaa glaciers (Fig. 7). By comparison, nSPF values are much more symmetric and range from −396 to 392 m/year with a greater distribution of positive (red) and negative (blue) nSPF rates throughout the region (Fig. 8). The effects of nSPF, whether positive or negative, extend across the full width of the glaciers, in direct contrast with the central localization of SPF values. Our findings demonstrate that changes in the mass balance and strain rates dominate regional surface elevation changes while advection plays a much smaller role.

On local scales, our methods can be used to evaluate the complementary nature of advective and strain rate processes on the vertical flow of ice. The upper reaches of the Seward Glacier flow northeast to southwest (Fig. 9) with a profile of surface elevations shown above each panel. Surface velocities are greatest in the upper reaches and slow downglacier (panel b). SPF rates are greatest in the northeast corner (panel c), coincident with the highest magnitude of horizontal velocities (panel b) and a steep surface slope. High vertical SPF rates also appear further downglacier in regions with steep surface slopes. Conversely, SPF is minimized along shallow slopes or flat surfaces with the reduced horizontal flow. These patterns illustrate the effects of horizontal speed

and surface slopes on advection processes. Similarly, large nSPF components appear along slower flowing zones in this area (panel d) where the glacier flows around a bend. These panels illustrate how different processes drive surface elevation changes in this region. As such, we use our measurements to characterize the dominant processes in vertical ice flow that control ice thickness variations within our study.

Our results show several interesting patterns. Comparing the total magnitude of 3D flow (Fig. 4) against the SPF (Fig. 7) and nSPF (Fig. 8), reveals a dichotomy between advective and strain rate-driven surface elevation variations along lower Hubbard Glacier. Negative SPF values indicate advection drives surface elevations lower here, while positive nSPF values drive surface elevations higher, particularly along the western edge, where the Hubbard and Valerie glaciers converge, and strain rates are most likely to be dominant. Along the Malaspina glacier, vertical flow is dominated by nSPF while SPF is minimal. Along the outer apron, SPF is close to zero, and nSPF decreases. Total velocities are low, suggesting smaller advective and strain rate components, which leaves surface mass balance as the primary driver of surface elevation changes, approximately −3 m/year during our observation period. The dominance of ablation here is also supported by the nearly vertical downward motion of flow in the lower 8 km of the profile in Fig. 6. Further up the profile, along the Seward glacier, fast flow leads to large SPF and nSPF rates, both of which contribute to surface lowering but with different spatial patterns.

Our methods can be quite informative for surge-type glaciers in the region. Along the lower reaches of the Klutlan Glacier, profile AB (Figs. 4-5) shows downward flow at 34–38 km segment along the profile (around P8) and upward flow at 40–48 km segment (around P9), when averaged over the entire Sentinel-1 record. However, the time series of displacement in Fig. 10 shows that this motion was episodic and occurred almost entirely during the second half of 2017 and the first half of 2018. Klutlan Glacier has a 30 (Meier and Post 1969) to 60-year surge cycle (Driscoll, 1980). It surged in the early 1960s (Driscoll, 1980) and began another surge in 2014 (Altena et al. 2019). Our records capture the last year of surge activity along this glacier. Our records also show the last six months of surge activity along the Walsh Glacier (P11) that was initiated before 2015 (Fu and Zhou 2020). These results demonstrate how the use of ascending and descending data to create a dense observational record can be used to evaluate the horizontal and vertical flow variations related to ice dynamics on surge-type glaciers (e.g. Fig. 5).

A signal-to-noise ratio (SNR) criterion was used to select coherent scatterers. Each range and azimuth offset products were computed independently of others, preventing the propagation of errors. Yet, time series produced from individual products demonstrate remarkable consistency and high precision. It is worth noting that while these results seem credible, the exact scattering mechanism (single/double bounce or volume scattering) and the reflective surface location at depth remain least understood and must be investigated further. Previous studies for this region suggest that the C-band SAR penetrates about four meters of the glacier's firn in dry conditions (Rignot et al. 2001). Conditions likely varied both seasonally and spatially. In Eq. (2) we neglect the vertical profile of velocity. Follow-up studies should combine multi-band (i.e. X, C, and L-band) SAR and optical images to evaluate differences in flow velocities from different penetration depths.

In regions experiencing moderate downward motion, the magnitude of the vertical nSPF velocity increases rapidly during warm seasons (Fig. 11). In regions experiencing upward motion, the magnitude of the vertical nSPF velocity decreases during warm seasons. The downward flow pattern in the vertical nSPF component can be explained by air temperature fluctuations. However, air temperature fluctuations cannot explain the upward flow pattern. Overall, the distribution of regions experiencing submergent/emergent flow does not fit the idealized hypothesis that submergence should be occurring in the accumulation zone at high elevations and emergence in the ablation zone at low elevations. Submergence is predominant in this region.

6. Conclusions

The method presented here can be used both for reconstructing the processes that drive surface elevation changes of glaciers worldwide using over 30 years of archived SAR data and for near real-time monitoring of these glaciers using rapid revisit SAR data from satellites, such as Sentinel-1 (6 days revisit period) and forthcoming NISAR (12 days revisit period).

The SAR-derived flow displacements time series should be interpreted with caution since they do not represent typical displacement time series as measured, for example, with GNSS. However, these MSBAS time series from approximately three years demonstrate that short and long-term variability in magnitude and direction of glacier flow can be significant. Utilizing flow velocity estimates from limited-duration geodetic campaigns of any kind is almost certainly biased and should be interpreted with caution.

This technique can compute a 3D or 4D flow displacement time series. The SPF and nSPF components can be derived from the vertical component for delineating advection from strain rate-driven processes. However, since basal sliding is not the only process that governs advection at the local scale, using the slope of a DEM as a proxy for estimating advection can be inaccurate in some regions, resulting in misclassification of the SPF component (or rather advection in general) for nSPF. The nSPF component can be used for computing either mass balance or strain rate variations if one of these two parameters is known from the external observations. The software implementation of this technique is made freely available to the research community.

Supplementary data to this article can be found online at https://doi.org/10.1016/j.rse.2021.112343.

Declaration of Competing Interest

The authors declare that they have no known competing financial interests or personal relationships that could have appeared to influence the work reported in this paper.

The authors declare the following financial interests/personal relationships which may be considered as potential competing interests.

Acknowledgements

We thank the European Space Agency for acquiring and the National Aeronautics and Space Administration (NASA) and ASF for distributing Sentinel-1 SAR data. Figures were plotted with GMT and Gnuplot software. Modeling was performed with R software. The work of Sergey Samsonov was supported by the Canadian Space Agency through the Data Utilization and Application Plan (DUAP) program. The work of Kristy Tiampo was supported by CIRES, University of Colorado Boulder. The work of Ryan Cassotto was supported by NASA Grant No. 80NSSC17K0017. The processing code will be made available upon request and published on the corresponding author's website http://insar.ca.

References

Abrams, M., Crippen, R., Fujisada, H., 2020. ASTER Global Digital Elevation Model (GDEM) and ASTER Global Water Body Dataset (ASTWBD). Remote Sens. 12 https://doi.org/10.3390/rs12071156.

Altena, B., Scambos, T., Fahnestock, M., Kääb, A., 2019. Extracting recent short-term glacier velocity evolution over southern Alaska and the Yukon from a large collection of Landsat data. Cryosphere 13, 795–814. https://doi.org/10.5194/tc-13-795-2019.

Amundson, J.M., Truffer, M., 2010. A unifying framework for iceberg-calving models. J. Glaciol. 56, 822–830. https://doi.org/10.3189/002214310794457173.

Bartholomew, I., Nienow, P., Mair, D., Hubbard, A., King, M., Sole, A., 2010. Seasonal evolution of subglacial drainage and acceleration in a Greenland outlet glacier. Nat. Geosci. 3, 408–411. https://doi.org/10.1038/ngeo863.

Beedle, M.J., Menounos, B., Wheate, R., 2014. An evaluation of mass-balance methods applied to Castle creek Glacier, British Columbia, Canada. J. Glaciol. 60, 262–276. https://doi.org/10.3189/2014JoG13J091.

Berthier, E., Vadon, H., Baratoux, D., Arnaud, Y., Vincent, C., Feigl, K., Remy, F., Legresy, B., 2005. Surface motion of mountain glaciers derived from satellite optical imagery. Remote Sens. Environ. 95, 14–28. https://doi.org/10.1016/j.rse.2004.11.005.

Bolch, T., Pieczonka, T., Benn, D., 2011. Multi-decadal mass loss of glaciers in the Everest area (Nepal Himalaya) derived from stereo imagery. Cryosphere 5, 349–358. https://doi.org/10.5194/tc-5-349-2011.

Braithwaite, R., Zong, Y., 2000. Sensitivity of mass balance of five Swiss glaciers to temperature changes assessed by tuning a degree-day model. J. Glaciol. 46, 7–14. https://doi.org/10.3189/172756500781833511.

Burgess, E., Forster, R., Larsen, C., 2013. Flow velocities of Alaskan glaciers. Nat. Commun. 4. https://doi.org/10.1038/ncomms3146.

Cogley, J., Hock, R., Rasmussen, L., Arendt, A., Bauder, A., Braithwaite, R., Jansson, P., Kaser, G., Moller, M., Zemp, M., 2011. Glossary of Glacier Mass Balance and Related Terms, Tech. Rep. UNESCO-IHP, Paris, p. 2.

Driscoll, F.J., 1980. Formation of the neoglacial surge moraines of the Klutlan glacier, Yukon Territory, Canada. Quat. Res. 19–30. https://doi.org/10.1016/0033-5894(80)90004-6.

Fahnestock, M., Scambos, T., Moon, T., Gardner, A., Haran, T., Klinger, M., 2016. Rapid large-area mapping of ice flow using Landsat 8. Remote Sens. Environ. 185, 84–94. https://doi.org/10.1016/j.rse.2015.11.023.

Fialko, Y., Simons, M., Agnew, D., 2001. The complete (3-D) surface displacement field in the epicentral area of the 1999 MW7.1 Hector Mine Earthquake, California, from space geodetic observations. Geophys. Res. Lett. 28, 3063–3066. https://doi.org/10.1029/2001GL013174.

Fu, X., Zhou, J., 2020. Recent surge behavior of Walsh glacier revealed by remote sensing data. Sensors 20, 716. https://doi.org/10.3390/s20030716.

Gardelle, J., Arnaud, Y., 2012. Slight mass gain of Karakoram glaciers in the early twenty-first century. Nat. Geosci. 5, 322–325. https://doi.org/10.1038/ngeo1450.

Glen, J., 1955. The creep of polycrystalline ice. Proceed. Royal Soc. London Series A, Math Phys. Sci. 228, 519–538.

Goldstein, R.M., Engelhardt, H., Kamb, B., Frolich, R.M., 1993. Satellite radar interferometry for monitoring ice sheet motion: application to an Antarctic ice stream. Science 262, 1525–1530. https://doi.org/10.1126/science.262.5139.1525.

Gray, A., Short, N., Mattar, K., Jezek, K., 2001. Velocities and flux of the Filchner ice shelf and its tributaries determined from speckle tracking interferometry. Can. J. Remote. Sens. 27, 193–206. https://doi.org/10.1080/07038992.2001.10854936.

Gudmundsson, G., Bauder, A., 1999. Towards an indirect determination of the mass-balance distribution of glaciers using the kinematic boundary condition. Geografiska Annaler. Series A Phys. Geogr. 81, 575–583.

Hansen, P., O'Leary, D., 1993. The use of the L-curve in the regularization of discrete ill-posed problems. SIAM J. Sci. Comput. 14, 1487–1503.

Herman, F., Anderson, B., Leprince, S., 2011. Mountain glacier velocity variation during a retreat/advance cycle quantified using sub-pixel analysis of ASTER images. J. Glaciol. 57, 197–207. https://doi.org/10.3189/002214311796405942.

Immerzeel, W., Kraaijenbrink, P., Shea, J., Shrestha, A., Pellicciotti, F., Bierkens, M., de Jong, S., 2014. High-resolution monitoring of Himalayan glacier dynamics using unmanned aerial vehicles. Remote Sens. Environ. 150, 93–103. https://doi.org/10.1016/j.rse.2014.04.025.

Joughin, I., 2002. Ice-sheet velocity mapping: a combined interferometric and speckle-tracking approach. Ann. Glaciol. 34, 195–201. https://doi.org/10.3189/172756402781817941.

Joughin, I., Winebrenner, D., Fahnestock, M., 1995. Observations of ice-sheet motion in Greenland using satellite radar interferometry. Geophys. Res. Lett. 22, 571–574. https://doi.org/10.1029/95GL00264.

Joughin, I., Kwok, R., Fahnestock, M., 1998. Interferometric estimation of three-dimensional ice-flow using ascending and descending passes. IEEE Trans. Geosci. Remote Sens. 36, 25–37. https://doi.org/10.1109/36.655315.

Kaab, A., Berthier, E., Nuth, C., Gardelle, J., Arnaud, Y., 2012. Contrasting patterns of early twenty-first-century glacier mass change in the Himalayas. Nature 488, 495–498. https://doi.org/10.1038/nature11324.

Meier, M., Post, A., 1969. What are glacier surges? Can. J. Earth Sci. 6, 807–817. https://doi.org/10.1139/e69-081.

Michel, R., Rignot, E., 1999. Flow of Glaciar Moreno, Argentina, from repeat-pass shuttle imaging radar images: comparison of the phase correlation method with radar interferometry. J. Glaciol. 45, 93–100. https://doi.org/10.3189/S0022143000003075.

Minchew, B.M., Simons, M., Riel, B., Milillo, P., 2017. Tidally induced variations in vertical and horizontal motion on Rutford Ice Stream, West Antarctica, inferred from remotely sensed observations. J. Geophys. Res. Earth Surf. 122, 167–190. https://doi.org/10.1002/2016JF003971.

Mohr, J., Reeh, N., Madsen, S., 1998. Three-dimensional glacial flow and surface elevation measured with radar interferometry. Nature 391, 273–276. https://doi.org/10.1038/34635.

Palmer, S.J., Shepherd, A., Sundal, A., Rinne, E., Nienow, P., 2010. InSAR observations of ice elevation and velocity fluctuations at the Flade Isblink ice cap, eastern North Greenland. J. Geophys. Res. Earth Surf. 115 https://doi.org/10.1029/2010JF001686.

Reeh, N., Madsen, S.N., Mohr, J.J., 1999. Combining SAR interferometry and the equation of continuity to estimate the three-dimensional glacier surface-velocity vector. J. Glaciol. 45, 533–538. https://doi.org/10.3189/S0022143000001398.

Rignot, E., 1998. Fast recession of a West Antarctic glacier. Science 281, 549–551. https://doi.org/10.1126/science.281.5376.549.

Rignot, E., 2002. Mass balance of East Antarctic glaciers and ice shelves from satellite data. Ann. Glaciol. 34, 217–227. https://doi.org/10.3189/172756402781817419.

Rignot, E., Echelmeyer, K., Krabill, W., 2001. Penetration depth of interferometric synthetic-aperture radar signals in snow and ice. Geophys. Res. Lett. 28, 3501–3504. https://doi.org/10.1029/2000GL012484.

Samsonov, S., D'Oreye, N., 2012. Multidimensional time series analysis of ground deformation from multiple InSAR data sets applied to Virunga Volcanic Province. Geophys. J. Int. 191, 1095–1108. https://doi.org/10.1111/j.1365-246X.2012.05669.x.

Samsonov, S., 2019. Three-dimensional deformation time series of glacier motion from multiple-aperture DInSAR observation. J. Geod. 93, 2651–2660. https://doi.org/10.1007/s00190-019-01325-y.

Samsonov, S., D'Oreye, N., 2017. Multidimensional Small Baseline Subset (MSBAS) for two-dimensional deformation analysis: case study Mexico City. Can. J. Remote. Sens. 43 https://doi.org/10.1080/07038992.2017.1344926.

Samsonov, S., Dille, A., Dewitte, O., Kervyn, F., D'Oreye, N., 2020a. Satellite interferometry for mapping surface deformation time series in one, two and three dimensions: A new method illustrated on a slow-moving landslide. Eng. Geol. 266 (105), 471. https://doi.org/10.1016/j.enggeo.2019.105471.

Samsonov, S., Tiampo, K., Cassotto, R., 2020b. Measuring the state and temporal evolution of glaciers using SAR-derived 3D time series of glacier surface flow. The Cryosphere Discussion. https://doi.org/10.5194/tc-2020-257.

Sauber, J., Molnia, B., Carabajal, C., Luthcke, S., Muskett, R., 2005. Ice elevations and surface change on the Malaspina Glacier, Alaska. Geophys. Res. Lett. 32. https://doi.org/10.1029/2005GL023943.

Shepherd, A., Wingham, D.J., Mansley, J.A.D., Corr, H.F.J., 2001. Inland thinning of Pine Island glacier, West Antarctica. Science 291, 862–864. https://doi.org/10.1126/science.291.5505.862.

Strozzi, T., Luckman, A., Murray, T., Wegmuller, U., Werner, C.L., 2002. Glacier motion estimation using SAR offset-tracking procedures. IEEE Trans. Geosci. Remote Sens. 40, 2384–2391. https://doi.org/10.1109/TGRS.2002.805079.

Vaughan, D.G., 2006. Recent trends in melting conditions on the Antarctic peninsula and their implications for ice-sheet mass balance and sea level. Arct. Antarct. Alp. Res. 38, 147–152. https://doi.org/10.1657/1523-0430(2006)038[0147:RTIMCO]2.0.CO;2.

van de Wal, R.S.W., Boot, W., van den Broeke, M.R., Smeets, C.J.P.P., Reijmer, C.H., Donker, J.J.A., Oerlemans, J., 2008. Large and rapid melt-induced velocity changes in the ablation zone of the Greenland ice sheet. Science 321, 111–113. https://doi.org/10.1126/science.1158540.

Wegmuller, U., Werner, C., 1997. GAMMA SAR Processor and Interferometry Software, in: The 3rd ERS Symposium on Space at the Service of our Environment, Florence, Italy.